Article

Impact of Proton–Proton Collisions on the Cosmic-Ray Spectrum in Giant Clouds

Hao-Ran Ge [1] and Ruo-Yu Liu [2,3,*] ID

1   Kuang Yaming Honor School, Nanjing University, Nanjing 210023, China; 201240049@smail.nju.edu.cn
2   School of Astronomy and Space Science, Nanjing University, Nanjing 210023, China
3   Key laboratory of Modern Astronomy and Astrophysics (Nanjing University), Ministry of Education, Nanjing 210023, China
*   Correspondence: ryliu@nju.edu.cn

Abstract: Gamma-ray production by proton–proton (pp) inelastic collisions plays an important role in searching for cosmic-ray (CR) accelerators. Understanding the pionic gamma-ray production associated with giant molecular/atomic clouds is thus crucial to identify this process. In this work, we study the feedback of the pionic gamma-ray production to the CR distribution, by considering collision-induced energy loss on cosmic-ray protons in the dense core region of molecular clouds (MCs). We try to introduce a Monte Carlo simulation framework to quantify this effect, and present a detailed analysis to evaluate how pp collisions harden the cosmic-ray proton spectrum and the resulting gamma-ray spectrum in giant clouds.

Keywords: cosmic ray; gamma-ray emission; diffusion

1. Introduction

Cosmic rays (CRs) are charged particles from the universe, consisting mostly of protons. The CR spectrum presents a "knee" at a few PeV energy [1–5], probably representing the limit of the particle acceleration capacity of the major CR sources in the galaxy due to the energy-dependent escape of CRs from the galaxy [6]. The main source population contributing CRs around and beyond the knee is a long-standing puzzle in modern astrophysics. Hadronic interactions between a CR proton and matter can generate neutral pions π_0 that further decay into gamma rays $\pi^0 \rightarrow \gamma + \gamma$. Each generated photon carries about 10% of the energy of the parent proton. Therefore, ultrahigh-energy (UHE) (photons with energy above 100 TeV) emission can serve as a probe of accelerators of CRs around and above PeV energies.

The hadronic interaction highly depends on the density of the target matter. If giant molecular or atomic clouds appear in the vicinity of the CR accelerators, escaping CRs can illuminate clouds [7–10], which can reveal the accelerator. Also, the spectrum of gamma rays from the clouds may provide insights into particle acceleration at the source and the particle transport around the source. Recently, the Large High Altitude Air Shower Observatory (LHAASO) reported the discovery of a giant UHE gamma-ray bubble in the star-forming region Cygnus X [11], which was suggested to be an efficient CR factory [12,13]. The gamma-ray spectrum extends up to 2 PeV without showing a clear cutoff feature, suggesting the existence of a super-PeVatron. In addition to the extended bubble, LHAASO also identified two hotspots at the inner region of the bubble, with the spatial association of two giant molecular clouds of a few times of $10^6 \, M_\odot$ [11]. The gamma-ray spectrum index of molecular clouds (MCs) is (-2.87 ± 0.07), slightly harder than the spectral index

associated with the HI emission (-2.94 ± 0.12) and that of the inner bubble LHAASO J2027 + 4119 (-2.99 ± 0.07). There is no report of the detection of the MCs from Fermi-LAT at the GeV gamma-ray band. It may indicate the suppression of low-energy CR density in the MCs, likely due to their slow diffusion and cooling inside the MCs. Yang et al. [14] discovered a deficit of relatively low-energy gamma rays (with energy less than 2 GeV) from the position of the dense core of the Taurus and Perseus clouds. It was interpreted as the shielding of low-energy CRs from the core of MC due to the energy loss. Although at high energies this effect is less prominent than that at low energies, it would still be able to affect the observed gamma-ray spectrum associated with giant clouds if the particle diffusion is significantly suppressed inside the MC. In addition, there have been suggestions ascribing gamma-ray emission associated with MCs near supernova remnants to pp collisions of run-away CRs [15–17]. The hardening of the gamma-ray spectrum at low energies in these sources might be also (partially) related to the energy loss process.

In this work, we aim to perform a quantitative study about the diffusion of CRs with energies between 10 TeV and 1 PeV into a dense MC. We will pay attention to the spatial distribution and the spectra of CRs inside the MC when taking into account the energy loss. Note that Aharonian and Atoyan [7] derived a one-dimensional (1D) analytical solution of CR distribution with energy loss via proton–proton collisions, under the assumption of a homogeneous matter distribution around the accelerator. In our case, the cloud is located at a distance from the accelerator, so the analytical solution cannot be applied. Therefore, we will employ a Monte Carlo simulation to deal with the CR propagation.

The rest of this paper is organized as follows: in Section 2, we introduce our method for the simulation; in Section 3, we show the simulated CR proton distribution and calculate the gamma-ray emission. Finally, we discuss the result and give a conclusion in Section 4.

2. Methods

The diffusion coefficient of particles $D(E)$ generally follows a form of power-law relation $D(E) = D_0(E/E_0)^\kappa$, where κ is the dependence on energy, and D_0 and E_0 are the diffusion coefficients at the pivot energy E_0. The value of κ depends on the slope of the power spectrum of the turbulence. This value is $1/3$ for Kolmogorov-type turbulence [18], and $1/2$ for Iroshnikov–Kraichnan-type turbulence [19,20]. In our simulation, we employ a diffusion coefficient of $D(E) = 5 \times 10^{26}(E/1\,\mathrm{TeV})^{1/2}\mathrm{cm}^2/\mathrm{s}$, following the theoretical modeling performed in Ref. [11] for the Cygnus Bubble. The value of κ would influence the propagated spectrum but would not change our main conclusion. For simplicity, we approximate the CR diffusion process as Brownian motion with velocity equal to the speed of light c. The mean free path of particle $l_c(E)$ can be related to the diffusion coefficient by $l_c(E) = 3D(E)/c$. The time interval δt in the simulation is set such that $c\delta t = 0.1 l_c(E)$. The geometry of the model is shown in Figure 1. We establish a Cartesian coordinate system centered at the particle accelerator, and the center of the cloud is located in the z-axis. To save computation time and resources, we only simulate the propagation of particles within a cone of a half opening angle θ_0. Particles are injected homogeneously per unit solid angle into the cone. If a particle were to escape the cone from the boundary, we would assume another particle of the same energy and velocity entering the cone from the boundary at the other side considering the symmetry of the system, i.e.,

$$\theta_{\mathrm{new}} = 2\theta_0 - \theta \quad \phi_{\mathrm{new}} = \phi - \pi \quad r_{\mathrm{new}} = r \tag{1}$$

Note that θ_0 cannot be small because otherwise the transverse radius of the cone would be smaller than the mean free path of the particle. In the simulation, we take $\theta_0 = \pi/3$.
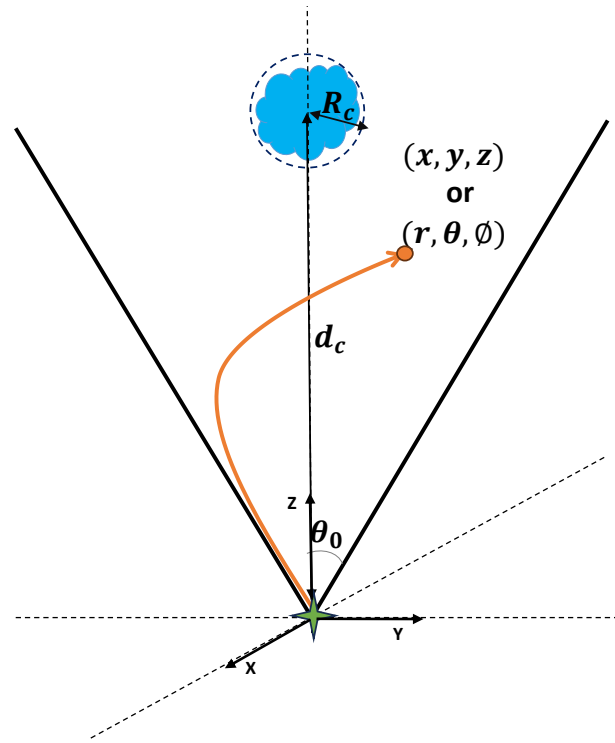
Figure 1. Schematic diagram of the conic model. θ_0 represents the half-opening angle of the cone. The center of the molecular cloud's location is at $(0, 0, d_c)$ and the injecting point is at $(0, 0, 0)$. CRs, represented by the orange circle, are injected isotropically from the vertex and propagate through a periodic boundary setup. This ensures a steady injection flux, with the molecular cloud positioned at a fixed distance to facilitate focused simulations of pp collisions.

To see the influence more clearly, we assume a large total mass of $5 \times 10^6 \, M_\odot$ for the cloud as the benchmark value. The density distribution of the molecular cloud follows that given in previous studies [21,22], i.e.,

$$\rho_H(R) = \frac{\rho_c}{(1 + (R/R_0)^2)^{n/2}}, \tag{2}$$

The density profiles given above are known solutions for the physical problem of self-gravitating gaseous clouds. Where we set $n = 4$ represents the exact solution for a self-gravitating isothermal cylinder [23]. And we set $R_0 = 10 \, \text{pc}$, and we find $\rho_c \simeq 2 \times 10^4 \text{cm}^{-3}$ to keep the total mass $M_{MC} = \int \rho(x, y, z) dx dy dz$ to be $5 \times 10^6 \, M_\odot$. Outside the cloud, we assume that there exists a homogeneous atomic hydrogen gas of density $1 \, \text{cm}^{-3}$. When a CR proton collides with a hydrogen nucleus in the cloud or ISM, the CR proton will lose about half of its original energy due to the production of pions ($\pi^0, \pi^\pm$). The collision possibility over a small time interval δt can be given by

$$\delta P = n_H c \sigma_{pp} \delta t \tag{3}$$

where σ_{pp} refers to the cross section of the pp collision, and can be parameterized by [24], and n_H is the number density of H:

$$\sigma_{pp} = \left[30.7 - 0.96\ln((E_p - 0.938)/E_{th}) + 0.18\ln((E_p - 0.938)/E_{th})^2 \right]$$
$$\times \left[1 - (E_{th}/(E_p - 0.938))^{1.9} \right]^3 \text{mb} \tag{4}$$

where $E_{\text{th}} = 0.938\,\text{GeV}$ is the threshold energy. The cross section is about 50 mb for protons between 10 TeV and 1 PeV, the energy range of interest in this work. In the simulation, a particle is abandoned if it has encountered interactions two times because its energy would then be significantly reduced. Note that the energy loss due to ionization is not important at such high energies because the cross section is very small.

The diffusion coefficient inside the MC may not be the same as that outside. On the one hand, given the presence of neutral molecules, the neutral-ion damping of turbulence may be efficient and lead to a fast diffusion of particles [25]. However, it has also been suggested that star formation inside giant MCs may drive turbulent motion of the gas and hence result in a slow diffusion of particles [26], which is supported by the discovery of Yang et al. [14]. We therefore parameterize the diffusion coefficient inside the MC by $D_{\text{MC}}(E) = \eta D(E)$, and the transition radius of the diffusion coefficient is set at $R_c = 2R_0$. In the following simulations, we will explore two cases with $\eta = 1$ and $\eta = 0.1$. And the basic setup of parameters in our simulation is summarized in Table 1.

Table 1. Simulation parameters.

Quantity	Symbol	Magnitude	Unit
Total Propagation time	T_{total}	1000	kyr
Half Opening Angle of the Cone	θ_0	$\pi/3$	Radian
Mass of Molecular Cloud	M_{MC}	5×10^6	$M_\odot$
Core Radius	R_0	10	pc
Cloud Distance from Accelerator	d_c	150	pc
Diffusion Coefficient outside the Cloud	$D(E_p)$	$5 \times 10^{26} \, (E_p/\text{TeV})^{1/2}$	cm^2/s
Transition Radius of $D(E_p)$	R_c	20	pc

3. Result

3.1. Instantaneous Injection

Let us first show the spatial distribution of proton number density in our simulation. With an instantaneous injection from a central point, the spatial probability distribution of a proton after diffusing a time of $t(\gg D/c^2)$ can be given by [27]

$$f_p(r,t) = \frac{1}{(4\pi Dt)^{3/2}} \exp\left(-\frac{r^2}{4Dt}\right) \tag{5}$$

In this solution, the energy loss of protons is not considered. For a cloud located at $r = d_c$ from the injection point (or accelerator), the higher-energy proton will arrive at the cloud earlier. The CR density inside the cloud would increase with time at the beginning, peak at a time $t \approx d_c^2/4D$, and then decrease. Since we focus on the CR distribution inside the MC, we denote the distance from the cloud center by R, which is not to be confused with r. In Figure 2, we show how the total number of protons within $R = 10$ pc changes with time in our simulation. Three energies of protons, 10 TeV, 100 TeV, and 1 PeV, are compared, with half a million particles simulated at each energy. We see that at early time $t = 100$ kyr, the front of the diffusing protons has not reached the cloud (corresponding to $t \ll d_c^2/4D$). At late time, when $t \gg d_c^2/4D$, the proton number density decreases with time. These behaviors are well consistent with what is described with the analytical formula above.
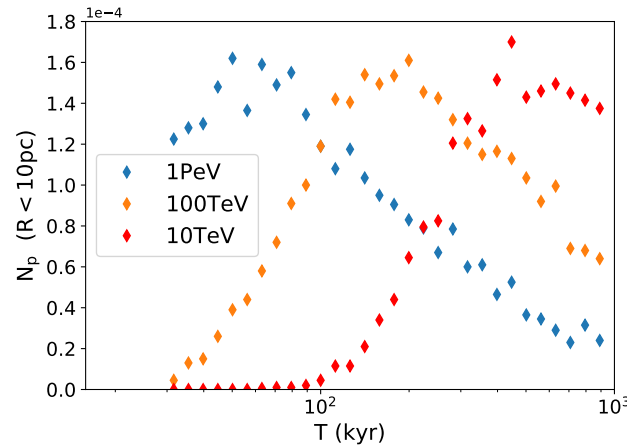
Figure 2. Evolution of normalized total proton counts N_p within 10 pc of the MC over time. The data highlight the temporal self-similarity of proton distributions across different energies, reflecting energy-dependent diffusion behaviors.

When we turn on the energy loss of protons in our simulation, the obtained spatial distribution of protons changes, especially for low-energy protons. To quantify the influence, we compare the simulations with and without considering the energy loss, deriving the 1D proton density profiles $f_p(E_p, R, t)$ (with loss) and $f_{p,0}(E_p, R, t)$ (without loss). f_p is obtained by dividing the number of protons within a series of concentric spherical shells in our simulation by the volume of each shell. We then define the ratio of the proton density profile between these two scenarios as $\beta(E_p, R, t) \equiv f_p(E_p, R, t)/f_{p,0}(E_p, R, t)$.

As shown in Figure 3, the suppression of CR density due to inelastic pp collisions is very pronounced for 10 TeV CRs at the core region of the cloud. For 1 PeV protons, the density inside the core region is only slightly reduced due to the loss. This is because lower-energy protons need a longer time to penetrate inside the core region with smaller diffusion coefficient. To see this more clearly, let us consider that protons diffuse from $R + \Delta R$ to R in the cloud, where $R \gg \Delta R > l_c(E_p)$. The expected distance δl traveled by protons can be given by $\Delta l = 2R\Delta R/l_c(E_p)$, with a random walk approximation. The pp collision possibility in this process is then $\delta P = \sigma_{pp}\rho(R)\Delta l = c\sigma_{pp} \cdot \frac{2\rho(R)R\Delta R}{3D(E_p)}$. The average number of collisions experienced by a CR proton during the propagation from a radius R to the core region then reads

$$N_C = \int_0^R \delta P = \frac{2c\sigma_{pp}}{3D(E_p)} \int_0^R \rho(R')R'dR' \tag{6}$$

Clearly, N_C is related to the density profile of the MC. If we use the MC density profile given by Equation (2), we obtain $N_C = (c\sigma_{pp}R_0^2\rho_c/3D(E_p)) \cdot (1 - \frac{1}{(1+R^2/R_0^2)^{n/2-1}})$. With $n = 4$, we arrive at $N_C = (c\sigma_{pp}R_0^2\rho_c/3D(E_p)) \cdot (1 - \frac{1}{1+R^2/R_0^2})$. Given a propagation time t, the typical diffusion length is $R^2 = 4D(E_p)t$ (if the energy loss is not important). We then can obtain an approximate analytical form for N_C as

$$N_C = \frac{c\sigma_{pp}R_0^2\rho_c}{3D(E_p)} \cdot \left(1 - \frac{1}{1 + 4D(E_p)t/R_0^2}\right) \tag{7}$$
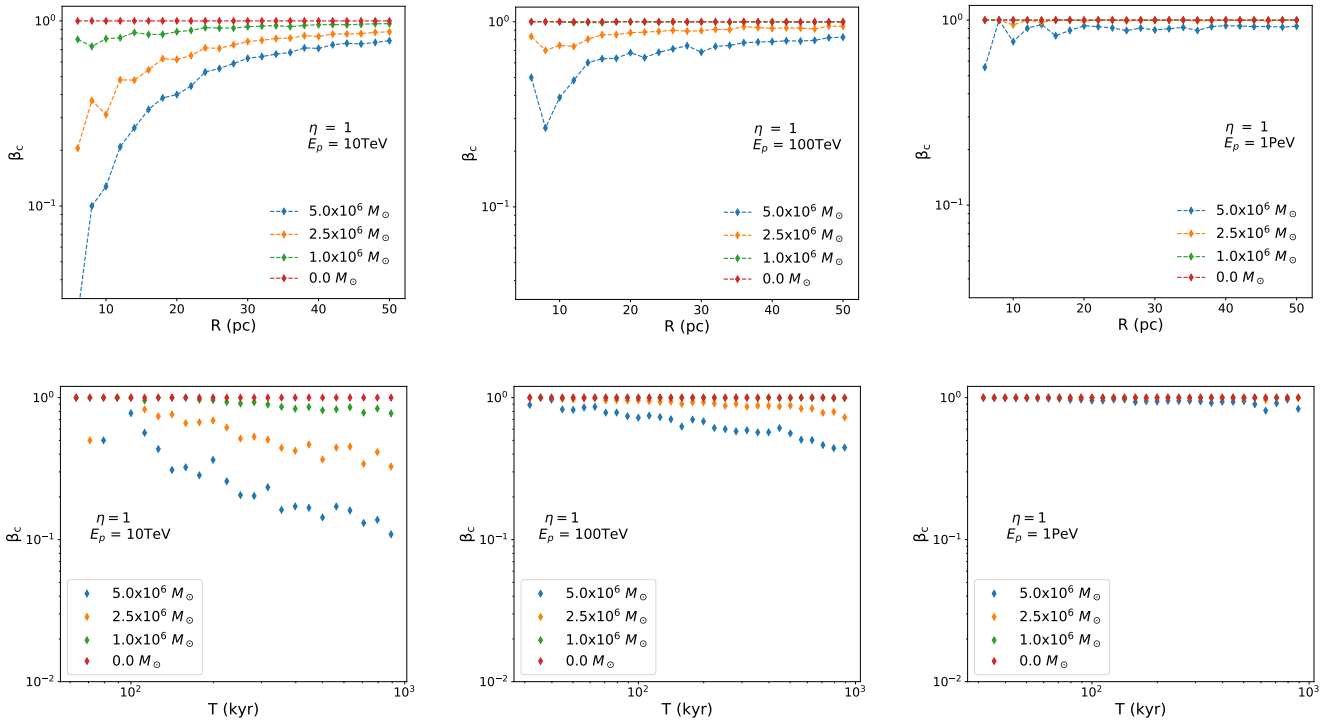
Figure 3. Suppression factor of proton density by the pp collision, i.e., $\beta_c(E, R, t)$, as a function of R (**top panels**) and t (**bottom panels**), for 10 TeV (**left**), 100 TeV (**middle**), and 1 PeV (**right**) protons. The propagation time is 1000 kyr for the top panels. In the bottom panels, β_c is calculated based on the particle number within $R = 10$ pc.

Given a sufficiently long time, i.e., $t \gg R_0^2/4D$, we have $N_C = N_{C,1} = c\sigma_{pp}R_0^2\rho_c/3D(E_p)$. We see that the number of collisions is not very dependent on the detailed form of the density profile of the MC in the envelop (i.e., n). Instead, the core density and the size of the core R_0 are important [8]. In addition, the influence of the diffusion coefficient can be explicitly seen. Substituting the benchmark values of parameters into the formula of $N_{C,1}$, we obtain $N_{C,1} = 6(E_p/10 \text{ TeV})^{-1/2}(M_{MC}/5 \times 10^6 M_\odot)$. For the proton energy of 10 TeV , 100 TeV and 1 PeV, the expected numbers of collisions are 6, 2, and 0.6 with $M_{MC} = 5 \times 10^6 M_\odot$, respectively. The fraction of remaining proton in the core can be estimated by $\exp(-N_{C,1}/2)$, where the factor 2 in the denominator is due to our abandoning a particle in the simulation after it has encountered two collisions as mentioned above. The analytical estimations, yielding $\beta_c \sim 0.05$ for 10 TeV, ~ 0.4 for 100 TeV and ~ 0.7 for 1 PeV, are roughly consistent with the values of β_c at the core region ($R \leq 10$ pc) shown in the top panels of Figure 3 with blue dots. We also show the evolution of β_c as a function time in bottom panels of Figure 3. If the diffusion coefficient inside the MC is further suppressed, the influence of the energy loss would be more pronounced. For $\eta = 0.1$ and $M_{MC} = 5 \times 10^6 M_\odot$, we see that the density of PeV protons is suppressed due to the energy loss even at 1 PeV as shown in Figure 4.
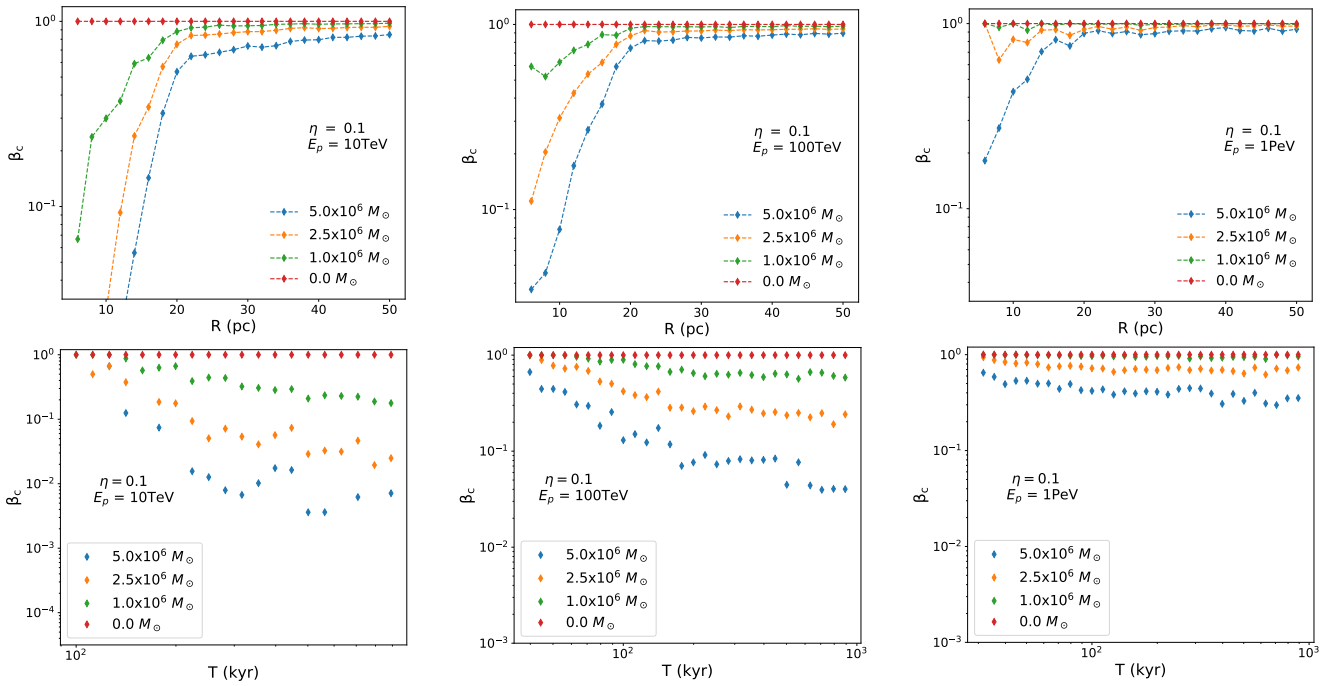
Figure 4. Same as Figure 3 but for $\eta = 0.1$.

It may be worth noting that N_C is related to the density profile (core density and the core radius) and the diffusion efficient $D_{\mathrm{MC}}(E)$ inside the MC according to Equation (7). The influence on the energy loss of particles from these two parameters has some degeneracy. The density profile of the target cloud may be estimated or constrained by observations of 21 cm line emission (for atomic clouds) [28] and observations of CO line emission (for MCs) [29]. If we can estimate the pp energy loss inside the cloud via the gamma-ray observations, the diffusion coefficient inside the MC may be derived.

3.2. Continuous Injection

For some CR sources such as young massive star clusters, CRs are supposed to be continuously accelerated and injected into the surrounding ISM. To obtain proton distribution in this case, we need to convolve Equation (5) with the proton injection history. Assuming a constant injection rate Q_0, the proton distribution is given by

$$g_p(E_p, r, t) \equiv \frac{dN_p}{dE} = Q_0 \int_0^{T_{\mathrm{total}}} dt' f_p(E_p, r, t') \tag{8}$$

In our simulation, we inject half a million particles and record their position after propagating every 5 thousand years. As such, we obtain f_p at a series of time from $t = 0$ to $t = T_{\mathrm{total}}$. We can then add the particle distribution at these time slices together to mimic the convolution process. Over a total simulation time of $T_{\mathrm{total}} = 1000\,\mathrm{kyr}$, we have equivalently 100 million particles in the simulation.

In Figure 5, we show the 1D proton density profile $g_p(R, t = T_{\mathrm{total}})$ for $E_p = 10\,\mathrm{TeV}$, $100\,\mathrm{TeV}$ and $1\,\mathrm{PeV}$, under the condition of $\eta = 1$, and different mass of MC. Here, we divide the density by a factor of 10^8, corresponding to a particle injection rate of $Q_0 = 1/T_{\mathrm{total}}$. g_p shown in Figure 5 can be also understood as the probability density distribution of proton after injection over a period of t. For $E_p = 10\,\mathrm{TeV}$, we see a slight decline in red points (without energy loss) at the core region. This is due to the insufficient propagation time for 10 TeV protons to reach the core. When considering energy loss (blue, orange, and green points), similar to the case of instantaneous injection, we see that the proton density is suppressed at 10 TeV and 100 TeV in the core region of the cloud due to the

energy loss, particularly for a large total mass (orange and blue points). For $\eta = 0.1$, as shown in Figure 6, even 1 PeV protons may suffer strong energy loss before reaching the core. Note that, for $\eta = 0.1$, we see a sharp break in the density profile appearing at $R = 20\,\text{pc}$. The position of the break corresponds to the transition radius of the diffusion coefficient $R_c = 2R_0 = 20\,\text{pc}$ within which the diffusion coefficient is 10% of the diffusion coefficient outside.
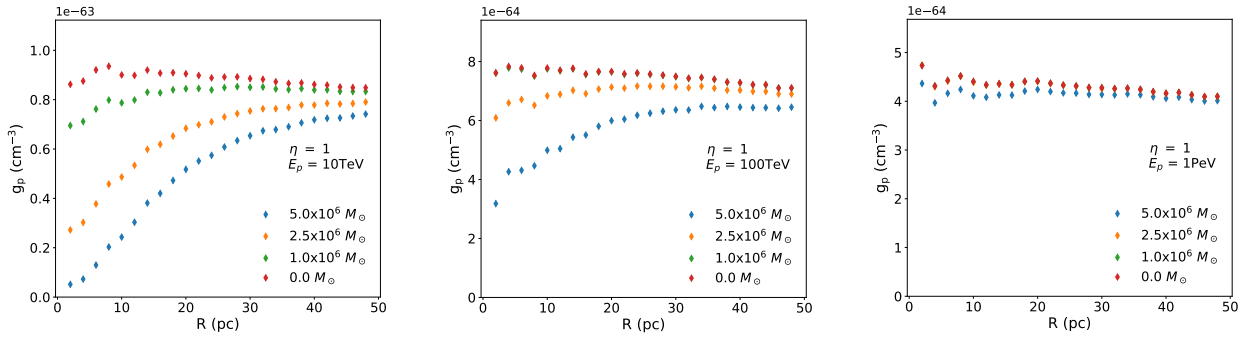

Figure 5. Normalized spatial distribution $g_p(E_p, R)$ of CR protons under continuous injection at 10 TeV (left), 100 TeV (middle), and 1 PeV (right). $\eta = 1$ is employed in this figure. The propagation time is 1000 kyr.
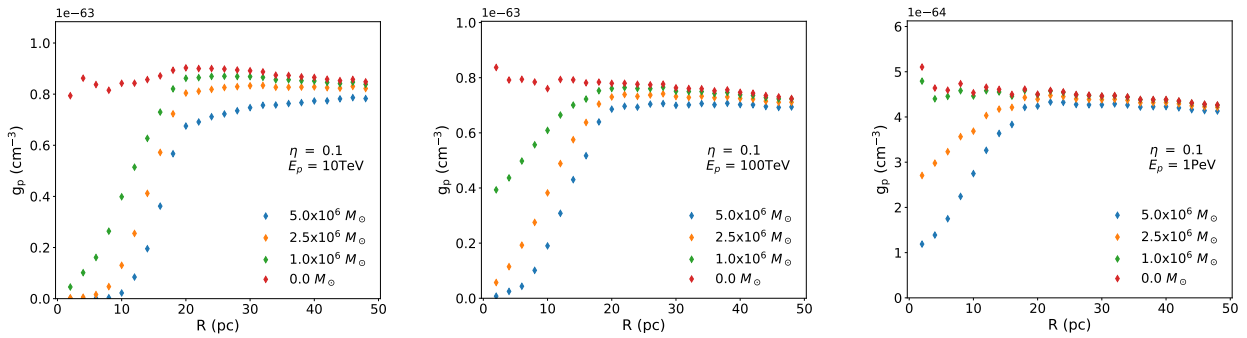

Figure 6. Same as Figure 5 but for $\eta = 0.1$.

In Figures 7 and 8, we present the proton number within the core region of the cloud (i.e., $R \leq 10\,\text{pc}$) at different energies for $\eta = 1$ and $\eta = 0.1$, respectively. Note that, at each energy, the numbers of total injected protons in the simulation are all 100 million. Therefore, it is equivalent to the propagated proton spectrum (in the form of $E_p dN/dE_p$) within the core region with a proton injection spectrum of $dN/dE_p \propto E_p^{-1}$ from the accelerator. The top-left panel shows the results without pp loss. We may see that the propagated spectrum is already hard at an early time (e.g., $t = 174\,\text{kyr}$). Comparing it with other three panels, we see that the *pp* energy loss hardens the spectrum at low energies. This is the opposite to the leptonic scenario, in which radiative cooling softens the particle spectrum.
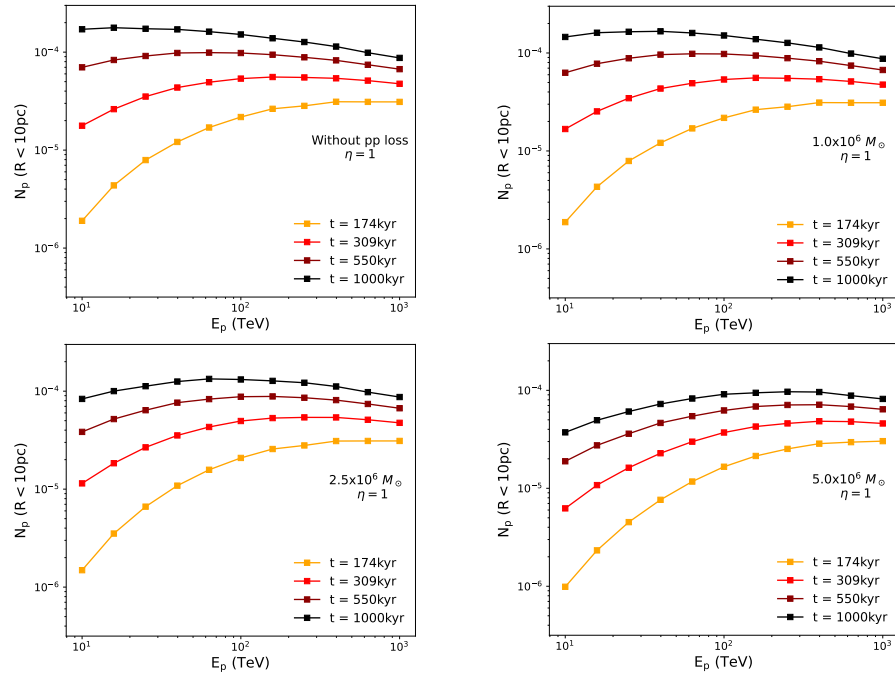
Figure 7. Total proton counts within 10 pc of the MC core for various masses and diffusion coefficients $\eta = 1$. Colored lines represent different propagation times, illustrating how pp collisions increasingly affect low-energy protons as the cloud mass increases.
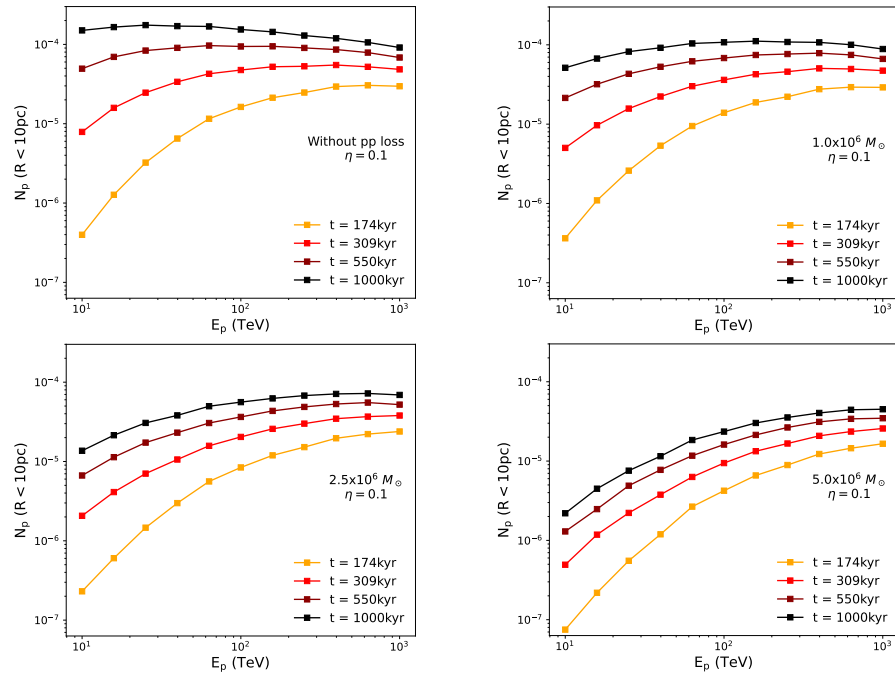

Figure 8. Same as Figure 7 but for $\eta = 0.1$.

3.3. Gamma-Ray Spectrum

Now, we look into the hadronic gamma-ray spectrum generated inside the MC. The gamma-ray emissivity $q_\gamma(E_\gamma, x, y, z)$ in a certain point of coordinate (x, y, z) can be calculated by the following semi-analytical method [24,30], which is mainly determined by the spatial and energy distribution of CR protons $g_p(E_p, R)$, and the molecular gas density $n_H(R)$. The formula can be given by

$$q_\gamma(E_\gamma, x, y, z) \equiv \frac{dN}{dE_\gamma dt dV} = c n_H(x, y, z) \kappa_{pp} \int g_p(E_p, x, y, z) \frac{d\sigma_{pp}^\gamma}{dE}(E_p, E_\gamma) dE_p, \quad (9)$$

where $d\sigma_{pp}^\gamma/dE$ represents the differential cross section of pp collisions for gamma-ray production. κ_{pp} is the inelasticity of the pp collision, which is about 0.5. Typically, gamma-ray photons generated from pp collision carry about 10% of the parent proton's energy, so the generated the gamma-ray spectrum basically follows the proton spectrum. On the other hand, in our case, at a position closer to the core region, the proton spectrum becomes harder and the target density becomes higher. In other words, the generated gamma-ray spectrum is harder at the position, where the emissivity is higher. As a consequence, the summed gamma-ray spectrum from the entire cloud would be harder than the average proton spectrum over the entire cloud. In Figure 9, we show the 1D radial profile of gamma-ray emissivity at different energies with $\eta = 1$ and $\eta = 0.1$. Apparently, the emissivity at the core region is suppressed and the suppression is more pronounced for lower-energy protons.
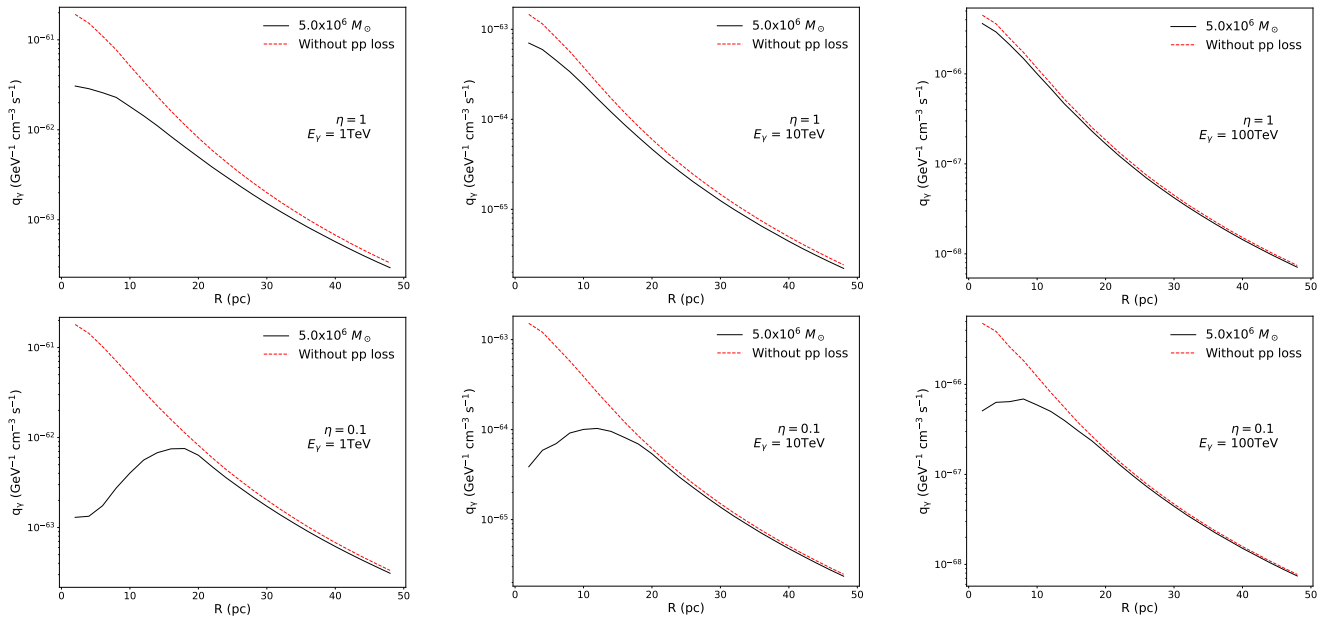

Figure 9. The figure shows the spatial distribution of γ emissivity $q_\gamma(E_\gamma, r)$. The upper pictures show the situation in $\eta = 1$. And the lower pictures show the situation in $\eta = 0.1$. The red dotted line represents the situation when the pp energy loss is not considered, while the black dashed line represents the existence of pp energy loss. The propagation time we set as $T = 1000$ kyr.

We also show the gamma-ray spectrum integrated over the core region in Figure 10. In this figure, we assume the injection spectrum of proton to be $Q_p(E_p) = Q_0 E_p^{-2}$, which is a typical spectrum expected from shock acceleration. The approximate spatial distribution of the density of propagated protons can be obtained simply with $N_p(E_p, R, t) = g(E_p, R, t)E_p Q_p(E_p)T_{\text{total}}$, noting that $g(E_p, R)$ has been already re-scaled so that it can be understood as a probability distribution function of protons after propagating a period of t. From Figure 10, we see more clearly the influence of the pp energy loss on the gamma-ray spectrum. For example, in the top-left panel, where $\eta = 1$ and $M_{\text{MC}} = 10^6 M_\odot$, the influence of the energy loss is not very strong. We see initially the spectrum is hard at low energies because most of the low-energy ($\sim$10 TeV) protons have not arrived at the core. As time goes, low-energy protons arrive, and the gamma-ray spectrum becomes softer and softer. If we see the bottom-right panel with $\eta = 0.1$ and $M_{\text{MC}} = 5 \times 10^6 M_\odot$, which is most affected by the energy loss, the low-energy spectrum is slightly harder in the first time slice ($t = 174$ kyr), and the spectral shape almost does not soften much as time goes. This may provide an explanation as to why Fermi-LAT does not see the gamma-ray hotspots associated with CO clumps as revealed by LHAASO in the Cygnus Bubble region.
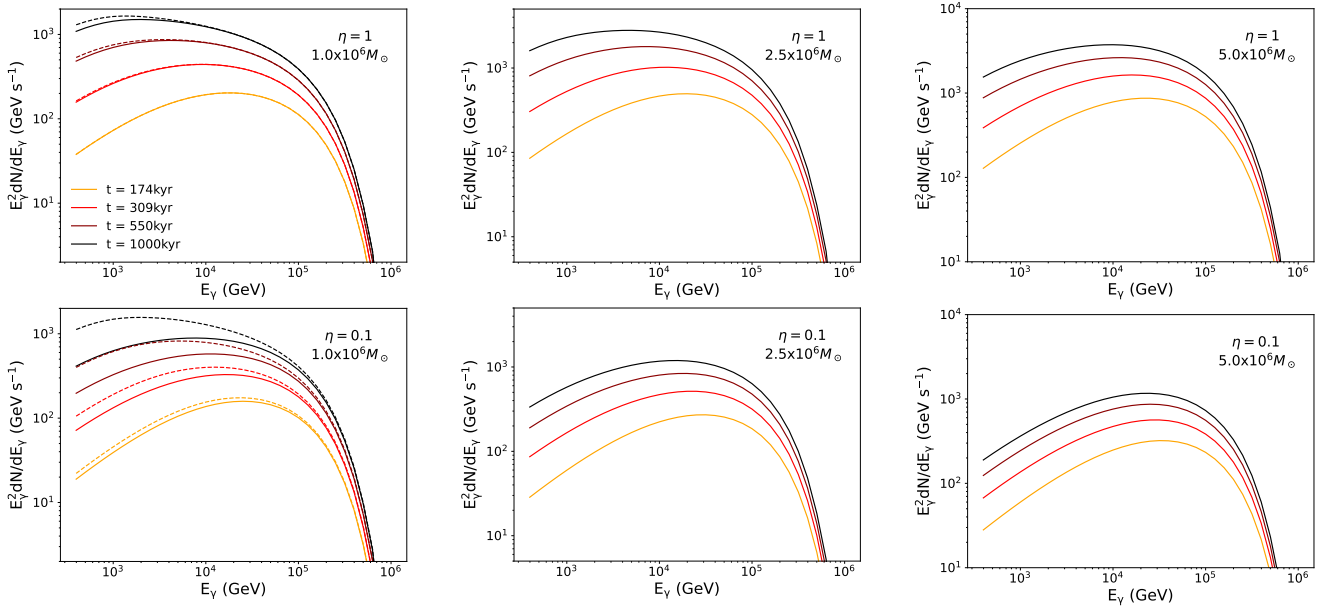
Figure 10. Temporal evolution of gamma-ray energy spectra $E_\gamma^2 dN/dE_\gamma$ within 10 pc of the molecular cloud core for various cloud masses. The upper panels show the spectra for $\eta = 1$, while the lower panels show $\eta = 0.1$. Dashed curves compare the case without considering pp energy loss. Since the proton distribution will not depend on the cloud mass if the energy loss is neglected, we only show dash curves in the top-left and bottom-left panels. The colored lines mean the different propagation times t shown in the top-left panel.

4. Discussion and Conclusions

To summarize, we studied the influence of the energy loss of CR protons induced by *pp* collisions during their penetration in the the core of giant molecular (or atomic) clouds. We approximated the diffusion of CR protons as Brownian motion, and employed the Monte Carlo simulation to obtain the spatial distribution of protons in the space after being injected into the space from a point-like accelerator, assuming both an instantaneous injection and a continuous injection. In light of LHAASO's study on the Cygnus Bubble region, we located a giant molecular cloud at 150 pc away from the accelerator and assumed a diffusion coefficient $D(E) = 5 \times 10^{26}(E/1\,\mathrm{TeV})^{1/2}\,\mathrm{cm^2/s}$. We found that the energy loss induced by *pp* collisions may significantly reduce the density of CR protons in the core region of the cloud.

The particle diffusion coefficient inside the cloud is uncertain, and the total mass, size, and density at the core vary from case to case. We derived an analytical relation, $N_{\mathrm{C},1} = c\sigma_{pp}R_0^2\rho_c/3D_{\mathrm{MC}}(E)$ with R_0 and ρ_c the size and density of the core respectively, to roughly estimate the expected number of *pp* collisions of a CR proton during the penetration into the core given a sufficient time ($t \gg R_0^2/D_{\mathrm{MC}}$). Since a particle is discarded in the simulation if it encounter collisions two times, the remaining fraction of CR protons in the core region can be estimated by $\exp(-N_{\mathrm{C},1}/2)$. This analytical estimation is insensitive to the density profile of the cloud but mainly depends on the properties of the core of the cloud. If the density profile of the cloud is well known, we may also use the gamma-ray observation to derive the diffusion coefficient inside the cloud, which can shed light on the properties of turbulence inside the cloud. We further calculated the pionic gamma-ray spectrum from the cloud, and found that the low-energy gamma-ray spectrum may be significantly hardened and the peak in the spectrum may be shifted to higher energy due to the energy loss.

We note that the propagation effect may also lead to a hard gamma-ray spectrum. Indeed, if the cloud is far from the particle accelerator, higher-energy particles may arrive

at the cloud while lower-energy particles may not because of the energy dependence of the diffusion coefficient. It is not easy to distinguish the energy loss effect from the propagation effect, if we observe a hard gamma-ray spectrum associated with a giant cloud. One possible way of distinguishing these two cases would be search whether a cloud located farther away from the accelerator is illuminated. In the propagation effect case, such a cloud is not expected to be illuminated but it is in the energy-loss-effect case. Of course, the existence of such a cloud is not guaranteed. Another potential difference between these two scenarios is the synchrotron radiation of secondary electrons/positrons co-produced with gamma rays. If the energy loss effect is important, the *pp* collision must be very efficient at relatively low energies, and the interactions between CR protons and the cloud must have started quite a long time ago. In contrast, if the hard gamma-ray spectrum is due to the propagation effect, the secondary electrons/positrons produced in the cloud should also have a hard spectrum because protons of relatively low energies have not arrived yet. Therefore, the spectrum of secondary electrons/positrons generated in the energy-loss-effect case should be much softer than that in the propagation effect, and would be able to be distinguished with radio and X-ray observations. A detailed quantitative study of the radiation from co-produced secondary pairs is beyond the scope of this study and would be a future project.

We also note that the realistic propagation of CR in the interstellar magnetic field is more complicated than the Brownian motion, which represents the normal diffusion. In some numerical simulations, superdiffusion such as Richardson diffusion [31] and the Lévy-flight-like propagation [32] of particles are observed under certain conditions. The influence of these modes of propagation on the result may be studied in the future with a more sophisticated simulation.

Author Contributions: Conceptualization, R.-Y.L.; Methodology, H.-R.G. and R.-Y.L.; Software, H.-R.G.; Validation, H.-R.G. and R.-Y.L.; Formal analysis, H.-R.G. and R.-Y.L.; Investigation, H.-R.G. and R.-Y.L.; Resources, R.-Y.L.; Data curation, H.-R.G.; Writing—original draft, H.-R.G.; Writing—review and editing, R.-Y.L.; Visualization, H.-R.G.; Supervision, R.-Y.L.; Project administration, H.-R.G. and R.-Y.L. All authors have read and agreed to the published version of the manuscript.

Data Availability Statement: The simulated data in this work are available upon request.

Conflicts of Interest: The authors declare no conflicts of interest.

References

1. Glasmacher, M.A.K.; Catanese, M.A.; Chantell, M.C.; Covault, C.E.; Cronin, J.W.; Fick, B.E.; Fortson, L.F.; Fowler, J.W.; Green, K.D.; Kieda, D.B.; et al. The cosmic ray energy spectrum between 10^{14} and 10^{16} eV. *Astropart. Phys.* **1999**, *10*, 291–302. [CrossRef]

2. Antoni, T.; Apel, W.D.; Badea, A.F.; Bekk, K.; Bercuci, A.; Blümer, J.; Bozdog, H.; Brancus, I.M.; Chilingarian, A.; Daumiller, K.; et al. KASCADE measurements of energy spectra for elemental groups of cosmic rays: Results and open problems. *Astropart. Phys.* **2005**, *24*, 1–25. [CrossRef]

3. Amenomori, M.; Bi, X.J.; Chen, D.; Cui, S.W.; Danzengluobu; Ding, L.K.; Ding, X.H.; Fan, C.; Feng, C.F.; Feng, Z.; et al. The All-Particle Spectrum of Primary Cosmic Rays in the Wide Energy Range from 10^{14} to 10^{17} eV Observed with the Tibet-III Air-Shower Array. *Astrophys. J.* **2008**, *678*, 1165–1179. [CrossRef]

4. Aartsen, M.G.; Abbasi, R.; Ackermann, M.; Adams, J.; Aguilar, J.A.; Ahlers, M.; Ahrens, M.; Alispach, C.; Amin, N.M.; Andeen, K.; et al. Cosmic ray spectrum from 250 TeV to 10 PeV using IceTop. *Phys. Rev. D* **2020**, *102*, 122001. [CrossRef]

5. Cao, Z.; Aharonian, F.; Axikegu; Bai, Y.X.; Bao, Y.W.; Bastieri, D.; Bi, X.J.; Bi, Y.J.; Bian, W.; Bukevich, A.V.; et al. Measurements of All-Particle Energy Spectrum and Mean Logarithmic Mass of Cosmic Rays from 0.3 to 30 PeV with LHAASO-KM2A. *Phys. Rev. Lett.* **2024**, *132*, 131002. [CrossRef]

6. Giacinti, G.; Kachelrieß, M.; Semikoz, D.V. Escape model for Galactic cosmic rays and an early extragalactic transition. *Phys. Rev. D* **2015**, *91*, 083009. [CrossRef]

7. Aharonian, F.; Atoyan, A. On the emissivity of piˆ 0ˆ-decay gamma radiation in the vicinity of accelerators of galactic cosmic rays. *Astron. Astrophys.* **1996**, *309*, 917–928.

8. Gabici, S.; Aharonian, F.A.; Blasi, P. Gamma rays from molecular clouds. In *The Multi-Messenger Approach to High-Energy Gamma-Ray Sources*; Springer: Berlin/Heidelberg, Germany, 2007; pp. 365–371.

9. Gabici, S.; Aharonian, F.A.; Casanova, S. Broad-band non-thermal emission from molecular clouds illuminated by cosmic rays from nearby supernova remnants. *Mon. Not. R. Astron. Soc.* **2009**, *396*, 1629–1639. [CrossRef]

10. Fujita, Y.; Ohira, Y.; Tanaka, S.J.; Takahara, F. Molecular Clouds as a Probe of Cosmic-Ray Acceleration in a Supernova Remnant. *Astrophys. J. Lett.* **2009**, *707*, L179–L183. [CrossRef]

11. Cao, Z. et al. [LHAASO Collaboration]. An ultrahigh-energy γ-ray bubble powered by a super PeVatron. *Sci. Bull.* **2024**, *69*, 449–457.

12. Ackermann, M.; Ajello, M.; Allafort, A.; Baldini, L.; Ballet, J.; Barbiellini, G.; Bastieri, D.; Belfiore, A.; Bellazzini, R.; Berenji, B.; et al. A Cocoon of Freshly Accelerated Cosmic Rays Detected by Fermi in the Cygnus Superbubble. *Science* **2011**, *334*, 1103. [CrossRef] [PubMed]

13. Abeysekara, A.U.; Albert, A.; Alfaro, R.; Alvarez, C.; Camacho, J.R.A.; Arteaga-Velázquez, J.C.; Arunbabu, K.P.; Rojas, D.A.; Solares, H.A.A.; Baghmanyan, V.; et al. HAWC observations of the acceleration of very-high-energy cosmic rays in the Cygnus Cocoon. *Nat. Astron.* **2021**, *5*, 465–471. [CrossRef]

14. Yang, R.z.; Li, G.X.; Wilhelmi, E.d.O.; Cui, Y.D.; Liu, B.; Aharonian, F. Effective shielding of $\lesssim$10 GeV cosmic rays from dense molecular clumps. *Nat. Astron.* **2023**, *7*, 351–358. [CrossRef]

15. Ohira, Y.; Murase, K.; Yamazaki, R. Gamma-rays from molecular clouds illuminated by cosmic rays escaping from interacting supernova remnants. *Mon. Not. R. Astron. Soc.* **2011**, *410*, 1577–1582. [CrossRef]

16. Li, H.; Chen, Y. γ-rays from molecular clouds illuminated by accumulated diffusive protons - II. Interacting supernova remnants. *Mon. Not. R. Astron. Soc.* **2012**, *421*, 935–942. [CrossRef]

17. Zhang, H.M.; Liu, R.Y.; Su, Y.; Zhu, H.; Xi, S.Q.; Wang, X.Y. Fermi-LAT Detection of Extended Gamma-Ray Emission in the Vicinity of SNR G045.7-00.4: Evidence of Escaping Cosmic Rays Interacting with the Surrounding Molecular Clouds. *Astrophys. J.* **2021**, *923*, 106. [CrossRef]

18. Kolmogorov, A. The Local Structure of Turbulence in Incompressible Viscous Fluid for Very Large Reynolds' Numbers. *DoSSR* **1941**, *30*, 301–305.

19. Iroshnikov, P.S. Turbulence of a Conducting Fluid in a Strong Magnetic Field. *AZh* **1963**, *40*, 742.

20. Kraichnan, R.H. Inertial-Range Spectrum of Hydromagnetic Turbulence. *Phys. Fluids* **1965**, *8*, 1385–1387. [CrossRef]

21. King, I. The structure of star clusters. I. an empirical density law. *Astron. J.* **1962**, *67*, 471. [CrossRef]

22. King, I.R. The structure of star clusters. III. Some simple dynamical models. *Astron. J.* **1966**, *71*, 64. [CrossRef]

23. Stodólkiewicz, J. On the Gravitational Instability of Some Magneto-Hydrodynamical Systems of Astrophysical Interest. Part III. *Acta Astron.* **1963**, *13*, 30–54.

24. Kafexhiu, E.; Aharonian, F.; Taylor, A.M.; Vila, G.S. Parametrization of gamma-ray production cross sections for p p interactions in a broad proton energy range from the kinematic threshold to PeV energies. *Phys. Rev. D* **2014**, *90*, 123014. [CrossRef]

25. Cesarsky, C.J.; Volk, H.J. Cosmic Ray Penetration into Molecular Clouds. *Astron. Astrophys.* **1978**, *70*, 367.

26. Li, G.X.; Burkert, A. Quantifying the interplay between gravity and magnetic field in molecular clouds - a possible multiscale energy equipartition in NGC 6334. *Mon. Not. R. Astron. Soc.* **2018**, *474*, 2167–2172. [CrossRef]

27. Syrovatskii, S.I. The Distribution of Relativistic Electrons in the Galaxy and the Spectrum of Synchrotron Radio Emission. *Sov. Astron.* **1959**, *3*, 22.

28. Pritchard, J.R.; Loeb, A. 21 cm cosmology in the 21st century. *Rep. Prog. Phys.* **2012**, *75*, 086901. [CrossRef]

29. Teyssier, D.; Hernandez, R.; Bujarrabal, V.; Yoshida, H.; Phillips, T. CO line emission from circumstellar envelopes. *Astron. Astrophys.* **2006**, *450*, 167–179. [CrossRef]

30. Kelner, S.R.; Aharonian, F.A.; Bugayov, V.V. Energy spectra of gamma rays, electrons, and neutrinos produced at proton-proton interactions in the very high energy regime. *Phys. Rev. D—Part. Fields, Gravitation, Cosmol.* **2006**, *74*, 034018. [CrossRef]

31. Maiti, S.; Makwana, K.; Zhang, H.; Yan, H. Cosmic-ray Transport in Magnetohydrodynamic Turbulence. *Astrophys. J.* **2022**, *926*, 94. [CrossRef]

32. Zhang, C.; Xu, S. Numerical Testing of Mirror Diffusion of Cosmic Rays. *Astrophys. J. Lett.* **2023**, *959*, L8. [CrossRef]